**Revision 2 of manuscript 8171R for American Mineralogist**

# Oxidation of arcs and mantle wedges by reduction of manganese in pelagic sediments during seafloor subduction

**Shuguang Song[1*], Shiting Ye[1], Mark B. Allen[2], Yaoling Niu[2], Weidong Sun[3], Lifei Zhang[1]**

*1 MOE Key Laboratory of Orogenic Belt and Crustal Evolution, School of Earth and Space Sciences, Peking University, Beijing 100871, China*

*2 Department of Earth Sciences, Durham University, Durham DH1 3LE, UK*

*3 Center of Deep Sea Research, Institute of Oceanography, Chinese Academy of Sciences, Qingdao 266071, China*

*Correspondent author: Shuguang Song

Email: sgsong@pku.edu.cn

## ABSTRACT

Plate subduction links the Earth's surface and interior and reshapes the redox state of the Earth's mantle. Mantle wedges above subduction zones have high oxygen fugacity compared with other mantle reservoirs, but the cause is debated. Here we analyse high-pressure metamorphic rocks derived from ferromanganese pelagic sediments in the Qilian subduction complex, NW China. We show that progressive metamorphism is a process of reducing reactions, in which $Mn^{4+}$ is reduced to $Mn^{2+}$. On the global scale, such reactions would release significant amounts of oxygen (~$1.27\times10^{12}$ g $year^{-1}$), estimated from the global flux of MnO in sediments passing into subduction zones. This budget is sufficient to raise the oxygen fugacity of the mantle wedge, hence arc magmas, to a higher level than other mantle reservoirs. In contrast, ferric iron ($Fe^{3+}$) enters hematite, aegirine and garnet, without valence change, and plays little role in the oxidation of the mantle wedge. $Fe^{3+}$ remains stable to depths of >100 km, but will transfer to the deeper mantle along with the subducting slab. The manganese reduction process provides a new explanation for high oxygen fugacity in the mantle wedge.

**Key words**: Ferromanganese pelagic sediments, high-pressure metamorphism, reductive reactions, subduction zone, mantle oxidation

## INTRODUCTION

Subduction zones are key places for understanding the dynamics of the Earth, and play an important role in the oxidation state and recirculation of oxygen and water (Wood et al, 1990; Frost and McCammon, 2008; Evens, 2012a; Kelley, 2009; Debret et al., 2014). It has been demonstrated that mantle wedges above subduction zones are more oxidized than oceanic or ancient cratonic

mantle, by the high oxidation state of both island-arc tholeiites and peridotites from the mantle wedges (Arculus, 1985; Parkinson and Arculus, 1999; Evens and Tomkins, 2011; Richards, 2015; Bucholz and Kelemen, 2019). Redox reactions in oceanic subduction zones must play important roles in controlling the oxidation state of the mantle wedge and the generation of island-arc tholeiites, and also in dictating the circulation of oxygen during whole-mantle convection.

The major factors controlling mantle oxygen fugacity, including volatile-budgets and mineral assemblages, and how tectonic processes drive its secular evolution, are still debated (Kelley, 2009; Lee et al., 2010). Dehydration fluids produced by high-pressure metamorphism in subduction channels are thought to be responsible for the oxidation and partial melting of the mantle wedge (Brandon and Draper, 1996; Song et al., 2009; Foley 2011), either directly through addition of volatiles, or indirectly if hydrous fluids carry dissolved $Fe^{3+}$ or sulphate (Kelley et al., 2009; Malaspina et al. 2017). Previous work suggested that oxidized Fe, C and S in sediments, altered ocean crust, and partially serpentinised lithospheric mantle in the subduction zones could also be important elements in controlling the redox state of the mantle (Evans and Tomkins, 2011; Evans, 2012b; Debret, 2014; Bénard et al., 2018). However, large amounts of organic carbon and sulfides in pelagic sediments (Alt, 1995; Evens, 2012; Plank and Langmuir, 1998; Plank, 2014) are in a reduced state and may need extra oxygen, while carbonates and sulfates can be stable at depths greater than 100 km (Forst and McCammon, 2008; Wang et al., 2016). Li et al. (2020) demonstrated that slab-derived fluids provide negligible sulfate to oxidize the sub-arc mantle. Thus S may not play an important role as an oxidizer in subduction zones. Several aspects of the redox state in subduction zones remain unclear, notably (1) how to generate high $fO_2$ fluid and the quantification of fluid

fluxes, and (2) the behavior of $Fe^{3+}$ in subduction channels. The details of redox reactions in subduction zones are poorly known.

Ferromanganese (Fe-Mn) chert is a common pelagic sedimentary rock both on the modern ocean floor and in subduction-zone complexes preserved in orogenic belts. The majority of iron and manganese in oceanic sediments is held in Mn-rich polymetallic nodules/crusts and banded Fe-Mn layers developed in deep ocean basins (Bonatti and Nayudu, 1965). These rocks are carried to mantle depths during subduction, and interact with mantle wedge as redox factors (Thamdrup et al., 1994; Tumiati et al., 2015). In this paper, we present detailed petrologic studies of Mn-rich, high pressure metasedimentary rocks from a representative, exhumed, ancient subduction complex, to define the Mn mineral assemblages produced during subduction. We describe redox reactions for ferromanganese-rich rocks at high-pressure. We demonstrate that reduction of $Mn^{4+}$ to $Mn^{2+}$ during subduction releases significant oxygen and water, which will be the major factor for oxidation of the mantle at depths of 70-100 km. Conversely, we show that $Fe^{3+}$ plays very little role at shallow mantle depths, and is subducted to depths greater than 100 km.

# GEOLOGICAL SETTING AND PETROGRAPHY

The Qilian Orogen extends for ~1000 km between the Alashan block to the north and the Qaidam Block to the south. Form north to south, the Qilian Orogen can be subdivided into the North Qilian Accretionary Belt (NQAB), the Central Qilian Block (CQB), the South Qilian Accretionary Belt (SQAB), the North Qaidam ultrahigh-pressure metamorphic belt (NQUB) and the Qaidam Block (Song et al., 2014, 2017). The NQAB consists of two ophiolite belts, a magmatic arc belt and

high-pressure metamorphic complexes (Fig. 1a). The southern ophiolite belt consists of MORB-type ophiolite sequences with ages of 550-495 Ma, and ophiolites in the northern belt are SSZ-type and aged ~490–450 Ma (Song et al., 2013). The arc belt between the two ophiolite belts consists of mafic to felsic volcanic rocks and granitic plutons with zircon ages ranging from ~ 530 Ma to 440 Ma (Xia et al., 2012; Song et al., 2013). The high-pressure metamorphic rocks occur as three WNW-trending tectonic slices within arc-type volcanic rocks. The lawsonite eclogite and carpholite metapelite, with P-T conditions of 2.0–2.6 GPa and 450–550 °C with metamorphic ages of 500–460 Ma, provide convincing evidence for cold seafloor subduction with a low geothermal gradient (6–7 °C/km) in the early Paleozoic (Song et al., 2007; Zhang et al., 2007).

High-pressure metamorphosed Mn-rich siliceous rocks occur as lenticular and layered blocks intercalated with lawsonite-bearing eclogites, blueschist and serpentinite (Fig. 2a). Four types of Mn-rich siliceous rocks have been recognized, including (1) Mn-rich quartzitic schist (Fig. 1c), (2) Mn (Fe) nodule-bearing quartzite (Fig. 1d), and (3) banded aegirine-hematite-pyroxmangite quartzite (Fig. 1e,f). All these rocks show the protolith characteristics of pelagic sediments from a deep ocean basin.

The Mn-rich quartzitic schist occurs as foliated blocks and is composed of a mineral assemblage that includes garnet, sodic clinopyroxene, glaucophane, phengite, piedmontite, sursassite, ardennite, hematite and quartz (Fig. 2a,b), suggesting its protolith would have been Mn-rich clay. The Fe-Mn nodule-bearing quartzite consists of weakly-deformed quartzite with thin Mn-Fe oxide layers and nodules. The nodules are 3-10 cm in diameter and scattered randomly in the quartzite. Mn-silicate minerals, including garnet, pyroxmangite, and minor coombsite, appear as a pink-colored rims around the Mn (Fe) nodules (Fig. 2c). The aegirine-hematite quartzite occurs in the same blocks. It exhibits

banded structure with Fe-Mn oxide layers and aegirine-quartz layers. The bands are 0.5-10 cm in thickness and consist predominantly of random, euhedral hematite ($Fe_2O_3$) with minor sussexite [$Mn^{2+}BO_2(OH)$]. Aegirine is scattered within both quartz bands and hematite bands (Fig. 2d,e). The banded hematite-pyroxmangite quartzite was found in several Mn (Fe)-rich quartzite blocks. The bands are 2-20 cm in thickness and consist predominantly of interbedded layers of euhedral pyroxmangite (+ garnet) and hematite (Fig. 1e,f).

# ANALYTICAL METHODS AND RESULTS

The studied samples are summarised in Appendix Figs. DR1 and DR2. Polished thin sections were produced from representative pieces of studied samples, and these were examined in detail using a petrographic microscope. Mineral compositions were analysed on an electron-probe micro-analyzer (EPMA) (JEOL JXA-8100) at Peking University, operated at 15 kV acceleration voltage, with 20 nA beam current and 1–5 μm beam spot. Routine analyses were obtained by counting for 20s at peak and 5s on background. Synthetic silica (Si) and spessartine (Mn), natural sanidine (K), pyrope (Mg), andradite (Fe and Ca), albite (Na and Al) and rutile (Ti) served as standards. Ferric iron in minerals was determined based on the scheme of Droop (1987)

Raman analyses were conducted at the school of Earth and Space Science, Peking University. The Raman spectra were acquired using a HORIBA Jobin Yvon confocal LabRAM HR Evolution micro-Raman system. The system is equipped with a frequency doubled Nd:YAG green laser (532.06 nm), a 100× short-working distance objective, and a stigmatic 800 mm spectrometer with a 600 groove/mm grating. The laser power was 100 mW at the source. The confocal hole was set at 100 μm and the corresponding spectral resolution was ±0.7 cm−1. The laser spot size was focused to

2 μm. During the experiments, Raman spectra between 100 and 1800 $cm^{-1}$ were recorded, and accumulation times varied between 10 and 20 seconds.

**Garnet.** Garnet in the Mn-rich quartz schist exhibits skeletal, syn-kinematic crystals with orientated mineral inclusions of piedmontite, hematite and quartz (Fig. 2a). In the Fe-Mn quartzite, garnet is fine- to medium-grained (10-500 μm) and euhedral (Fig. 2c). All garnets have high MnO, medium CaO and FeOt, and low MgO (0.34-0.6) wt% (Fig. 3a, Appendix Table S1). FeOt in garnet is all $Fe^{3+}$ ($Fe^{3+}/\Sigma Fe = 1$) on the basis of formula calculations. Raman spectrum shows major bands of spessartine (358, 552, 906 $cm^{-1}$) with weak bands of andradite (517, 815, 847 $cm^{-1}$) (Fig. 4a).

**Sodic clinopyroxene.** Sodic clinopyroxene (Cpx) in the Mn-rich quartz schist occurs as colourless, anhedral grains and forms assemblages with quartz and Mn-rich minerals (Fig. 2b). It is composed of ~26-45 mol% of jadeite, and 45-50 mol.% of aegirine. Sodic Cpx in the banded Fe-Mn quartzite is light-green (Fig. 2d). It has extremely high aegirine content of 81-87 mol%, without jadeite (Fig. 3b and Appendix Table S2). These two kinds of Cpx show variable Raman spectra with characteristic bands of aegirine (Figs. 4b and 4c).

**Pyroxmangite.** Pyroxmangite occurs in the Fe-Mn quartzite as tabular and rectangular prismatic crystals with massive or coxcomb/radiated aggregates. It is nearly pure $MnSiO_3$ with minor Fe and Mg (Appendix Table S3). Raman microspectroscopic analysis yields the characteristic bands at 416, 669, 973 and 997 $cm^{-1}$ and weak bands at 331 and 871 $cm^{-1}$ (Fig. 4d).

**Piedmontite and Sursassite.** Piedmontite occurs as pink-colored, euhedral crystals in the Mn-rich quartz schist. It lies within the foliation with the assemblage garnet + clinopyroxene + Mn-epidote + glaucophane + phengite + quartz (Fig. 1b). Sursassite occurs as euhedral, red brown crystals in the Mn-rich quartz schist with other minerals. It contains high MnO (24.8-27.1 wt%) and low CaO (2.5-3.6 wt%) (Appendix Table S4). Raman spectra of piedmontite and sursassite show multiple characteristic bands of epidote-group due to their complicated components (Figs. 3e and 3f).

**Phengite.** Phengite occurs as 50–200 μm homogeneous flakes in equilibrium with garnet and clinopyroxene, which forms ~5 vol.% of the rock matrix in the Mn-rich quartz schist. Si-contents range from 3.43 to 3.47 Si atoms per formula unit based on 11 oxygen (Appendix Table S5).

**Fe oxide.** All iron oxides in the studied samples are exclusively hematite (Appendix Table S6). They occur as euhedral crystals in both matrix and in garnet, and as bands in the Fe-Mn quartzite (Fig. 1). Raman spectroscopy shows that these euhedral crystals are typical hematite ($Fe_2O_3$) with major bands at 228, 294, 412 and 497 $cm^{-1}$ (Fig. 3g).

**Ardennite-(As).** Ardennite occurs as golden-yellow, prismatic crystals together with garnet, glaucophane, piedmontite and sursassite in the Mn-rich quartz schist (Fig. 4f). The mineral was crystallographically and compositionally characterized by Ye et al. (2019). This mineral is enriched in As ($As_2O_5$ 5.0-7.9 wt%) with minor abundances of F, V and P. Raman spectrum show that the ardennite-(As) has complex characteristic peaks, probably indicating the presence of arsenate, MnO and $SiO_3$ bonds (Fig. 3h).

In summary, hematite and ardennite-(As), in the absence of magnetite, reveal that the studied samples were formed at conditions of extremely high oxygen fugacity ($fO_2$) above the hematite–magnetite (HM) buffer, up to ΔFMQ + 12.7 (Tumiati et al., 2015).

# DISCUSSION

## Reduction of Mn from $Mn^{4+}$ to $Mn^{2+}$ in subduction zones at depths of 60-100 km

The majority of manganese in deep marine sediments occurs as $Mn^{4+}$ in the mineral assemblage buserite ($Na_4Mn_{14}O_{27}\cdot 21H_2O$), birnessite ($(Na,Ca,K)_{0.5}(Mn^{4+},Mn^{3+})_2O_4\cdot 1.5H_2O$), vernadite ($(Mn^{4+},Fe^{3+},Ca,Na)(O,OH)_2\cdot nH_2O$), and todorokite ($(Ca,K,Na)(Mn^{4+},Mn^{3+},Al)_6O_{12}\cdot 3H_2O$ (Post, 1999; Rona, 2008). When seafloor subduction occurs, these Mn-Fe-rich sedimentary rocks go down the subduction zone and experience HP metamorphism, which in the Qilian orogen has been determined at conditions of P = 2.0-2.6 GPa and T = 450-550 °C (Song et al., 2007; Zhang et al., 2007; Wei and Song, 2008). According to the mineral assemblages described above, redox reactions of the Fe-Mn chert in the subduction zones may be defined as follows:

$$MnO_2\cdot H_2O + SiO_2 \rightarrow MnSiO_3 \text{ (pyroxmangite)} + H_2O + 0.5\ O_2^{\uparrow} \quad (1)$$

$$MnO_2\cdot H_2O + CO_2 \rightarrow MnCO_3 \text{ (rhodochrosite)} + 0.5O_2 + H_2O \quad (2)$$

$$(Ca,K,Na)(Mn^{4+}, Mn^{3+},Al)_6O_{12}\cdot 3H_2O + Fe_2O_3\cdot H_2O + SiO_2 \rightarrow (Ca,Mn^{2+})_2(Al,Fe^{3+})_2\ Si_3O_{12} \text{ (garnet)} + Na(Al,Fe^{3+})Si_2O_6 \text{ (sodic pyroxene)} + O_2^{\uparrow} + H_2O \quad (3)$$

$$(Mn^{4+},Fe^{3+},Ca,Na)(O,OH)_2\cdot nH_2O \text{ (vernadite)} + SiO_2 \rightarrow (Ca,Mn^{2+})_3(Al,Fe^{3+})_2Si_3O_{12} \text{ (garnet)} + Na[Fe^{3+}]Si_2O_6 \text{ (aegirine)} + O_2^{\uparrow} + H_2O \quad (4)$$

All manganese in our samples is in the $Mn^{2+}$ oxidation state, with minor $Mn^{3+}$ (in piedmontite and sursassite). These dehydration reactions represent a significant production and potential release of oxygen along with water from the deep marine minerals. These reactions occur in the shallow part of subduction zones at depths of about 60-80 km, and up to ~100 km for all $Mn^{3+}$ to $Mn^{2+}$ as decomposition of epidote-group minerals (e.g., piedmontite) takes place (e.g., Poli and Smith, 2001). Therefore, the $O_2$ and $H_2O$ released by Mn reduction reactions potentially plays an important role in the oxidation of subduction zones and mantle wedges.

## Global budget of oxygen released by Mn reduction during subduction

Manganese is the 10$^{th}$ most abundant element in the Earth's crust (Post, 1999). In Phanerozoic orogenic belts that preserve relicts of oceanic subduction zones, manganese chert (or Mn-ore deposits) occurs as residual blocks in high-pressure metamorphosed mélanges and ophiolite complexes. Besides the Qilian region, various grades of metamorphic Fe-Mn cherts have been reported in most oceanic subduction-zone complexes, e.g., subduction mélanges of the Alps (Frezzotti et al., 2014; Tumiati et al., 2015), the Otago accretionary mélange complex of New Zealand (Kawachi et al., 1983), the Franciscan complex (Huebner and Flohr, 1990), accretionary belts of Japan (Akasaka et al., 1988), the high-pressure metamorphic complex in Bohemian part of the Moldanubian Zone (Vrána, 2011), high-pressure/low-temperature complex at Bahia Mansa, Coastal Cordillera of south-central Chile (Willner et al., 2001), and, ophiolitic mélange zones of Turkey, Pakistan and Iran (Table 1).

In the present-day ocean floor, polymetallic Fe-Mn nodules cover more than 50% of the sea floor over large areas of the abyssal Pacific and Central Indian oceans (Rona, 2008). The total amount of

polymetallic Fe-Mn nodules (27–30% metallic manganese) lying on the sea floor surface was estimated at more than 1.5 trillion tonnes (Mero, 1965). Besides the Fe-Mn nodules, ca. $2\times10^{11}$ tonnes of Fe–Mn crusts occur as pavements and coatings on rocks at water depths of 400-7000 m (Hein et al., 2003; González, et al., 2010), with a varying range of 14.5-34 wt % metallic Mn. However, these Fe-Mn nodules and crusts only occur within less than 5 meters of the surface (Hein et al., 2013); they represent volumetrically a minor component of the subducted sediments. In present-day pelagic sediments, Mn mainly occurs in ferromanganese-rich brown clay layers, observed in ODP and DSDP drill cores (Plank and Langmuir, 1998; Plank, 2014). A rough estimate for MnO flux of global subducting sediment (GLOSS) given by Plank and Langmuir (1998) is $4.19\times10^{12}$ g year$^{-1}$, and increasing to $5.63\times10^{12}$ g year$^{-1}$ in the revised GLOSS-II (Plank, 2014). Given that all Mn in the pelagic brown clays, nodules and crust are predominantly in the $Mn^{4+}$ state (Post, 1999; Hein et al., 2003; März, et al. 2011), they would produce ca. ~$3.97\times10^{10}$ mole (or ~$1.27\times10^{12}$ g) of $O_2$ each year during subduction through reduction of $Mn^{4+}$ to $Mn^{2+}$ (i.e., Mn oxides to Mn-silicate phases), assuming complete conversion using GLOSS-II (Plank, 2014).

As the total length of subduction zones on Earth is ~51310 km (Bird, 2003), the average oxygen production rate is up to ~$2.475\times10^{13}$ g km$^{-1}$ my$^{-1}$. Assuming all the oxygen is used to oxidize the FeO into $Fe_2O_3$, it would produce ca. ~$2.47\times10^{8}$ g km$^{-1}$ year$^{-1}$, or ~$2.47\times10^{14}$ g km$^{-1}$ my$^{-1}$, of $Fe_2O_3$ in the mantle wedge, which would significantly increase the oxygen fugacity of the subarc mantle up to a higher level than any other mantle reservoir.

The released oxygen from the subduction zone to forearc and mantle wedge is also significant because it impacts the rate of oxygen fugacity increase.. There are many potential mechanisms for

oxygen transport, but we highlight three that are known to be significant contributors to the transportation of oxygen as follows. (1) The released oxygen oxidizes carbon to $CO_2$ and sulphur to $SO_4^{2-}$, (2) oxygen and water become supercritical fluids at high pressure and temperature, which increases the migration significantly (e.g. Ni et al., 2017), and (3) because the Mn-rich pelagic cherts are located in the upmost part of the subducted slab, their released fluids could be transported into the forearc and the mantle wedge as a result of proximity.

Therefore, these fluids provide an important and consistent source of oxidizers to the subduction channel and mantle wedge at the shallow part of subduction zones (Fig. 5). These processes are simple, but effective mechanisms to produce oxygen or oxidizing agents by reduction reactions of $Mn^{4+}$ to $Mn^{2+}$ in subduction zones.

## Function of $Fe^{3+}$ in subduction zones

Iron oxides and oxyhydroxides in marine environments in Fe-Mn nodules/crusts and banded iron formations are mainly goethite (α-FeOOH) and lepidocrocite (γ-FeOOH) with accessory minerals of carbonates, pyrite, rutile, ilmenite and chlorite (Post, 1999). Reactions of iron oxide in the subduction zones can be as a simple dehydration of goethite (FeOOH) to hematite as 2FeOOH = $Fe_2O_3$ + $H_2O$. During the reduction of Mn4+ to Mn3+ and Mn2+, Fe is typically present in the ferric state in hematite, aegirine and the Mn-epidote minerals, and even into garnet. These solid $Fe^{3+}$-bearing phases are difficult to dissolve in subduction-zone fluids (Evens and Tomkins, 2011), and thus play little role in the shallow part of subduction zones and the mantle wedge.

The ferric iron ($Fe^{3+}$) minerals in high-pressure rocks, such as hematite, aegirine and garnet, which in these rocks has a spessartine composition with minor andradite, can be stable beyond at least 100 km in subduction zones, even to the transition zone or the lower mantle (Bebout, 2007), which would provide a continuous potential oxidizer for the transition zone and the lower mantle.

## Implications

Progressive metamorphism of ferromanganese-rich sediments is a sequence of reducing reactions, and the valence change of Mn from +4 to +2 in the subduction zone is an important factor for mantle wedge oxidation and oxygen recirculation. Our study identifies the importance of Mn as a control on the redox state of the mantle wedge above subduction zones.

The estimated oxygen flux generated by progressive metamorphism of Mn-rich pelagic sediments could reach as high as ~$1.28\times10^{12}$ g each year, which may significantly alter the oxidation state of the mantle wedge, increasing it significantly..

All the ferric iron ($Fe^{+3}$) in the sediments is hosted by hematite, aegirine, piedmontite and garnet, and underwent little to no valence change. This permits the transportation of Fe into the deep mantle and where it plays very little role in changing the oxidation state of the sub-arc mantle wedge.

**Acknowledgments:** We thank G.M. Shu and X.L. Li for helps in EPMA analysis, and Y. Cui for help with Raman analysis. We thank Katy Evans for constructive suggestions on the early version of the manuscript. We also thank Hans-Peter Schertl, two anonymous reviewers, as well as Editor Callum J Hetherington, for their constructive comments, which significantly improved the quality of the paper.

This research is supported by the National Key Research and Development Program of China (2019YFA0708503), and National Natural Science Foundation of China (Grant Nos. 91955202).

## References

Akasaka, M., Sakakibara, M., and Togari, K. (1988). Piemontite from the manganiferous hematite ore deposits in the Tokoro Belt, Hokkaido, Japan. Mineralogy and Petrology, 38, 105-116.

Alt, J.C. (1995). Sulfur isotopic profile through the oceanic-crust — sulfur mobility and seawater-crustal sulfur exchange during hydrothermal alteration. Geology, 23, 585–588.

Arculus, R.J. (1985). Oxidation Status of the Mantle. Past and Present. Annual Review of Earth and Planetary Sciences, 13, 75-95.

Bebout, G.E. (2007). Metamorphic chemical geodynamics of subduction zones. Earth and Planetary Science Letters, 260, 373-393.

Bénard, A., Klimm, K., Woodland, A. B., Arculus, R. J., Wilke, M., Botcharnikov, R. E., Shimizu, N., Nebel, O., Rivard, C., and Ionov, D. A., 2018, Oxidising agents in sub-arc mantle melts link slab devolatilisation and arc magmas. Nature Communications, 9, 3500.

Bird, P., (2003). An updated digital model of plate boundaries, Geochemistry, Geophysics, Geosystems, 4(3), 1027.

Bonatti, E., and Nayudu, Y. R. (1965). The origin of manganese nodules on the ocean floor. American Journal of Science, 263, 17-39.

Brandon, A. D., and Draper, D. S. (1996). Constraints on the origin of the oxidation state of mantle overlying subduction zones: An example from Simcoe, Washington, USA. Geochimica Et Cosmochimica Acta, 60, 1739-1749.

Brown, P., Essene, E. J., and Peacor, D. R. (1978). The mineralogy and petrology of manganese-rich rocks from St. Marcel, Piedmont, Italy. Contributions to Mineralogy and Petrology, 67, 227-232.

Bucholz, C. E., and Kelemen, P. B. (2019). Oxygen fugacity at the base of the Talkeetna arc, Alaska. Contributions to Mineralogy and Petrology, 174(10), 79.

Debret, B., Andreani, M., Muñoz, M., Bolfan-Casanova, N., Carlut, J., Nicollet, C., Schwartz, S., and Trcera, N. (2014). Evolution of Fe redox state in serpentine during subduction. Earth and Planetary Science Letters, 400, 206-218.

Droop, G. R. T. (1987). Ageneral equation for estimating $Fe^{3+}$ microprobe analyses, using stoichiometric criteria. Mineralogical Magazine, 51, 431–435.

Evans, K.A. (2012). The redox budget of subduction zones. Earth-Science Reviews, 113, 11-32.

Evans, K.A., and Tomkins, A.G. (2011). The relationship between subduction zone redox budget and arc magma fertility. Earth and Planetary Science Letters, 308, 401-409.

Evans, K. A., Elburg, M. A., and Kamenetsky, S. (2012). Oxidation state of subarc mantle. Geology, 40, 783-786.

Foley, S. F. (2011). A Reappraisal of Redox Melting in the Earth's Mantle as a Function of Tectonic Setting and Time. Journal of Petrology, 52, 1363-1391.

Frezzotti, M.-L., Huizenga, J.-M., Compagnoni, R. and Selverstone, J. (2014). Diamond formation by carbon saturation in C–O–H fluids during cold subduction of oceanic lithosphere. Geochimica Et Cosmochimica Acta, 143, 68-86.

Frost, D.J., and McCammon, C.A. (2008). The Redox State of Earth's Mantle. Annual Review of Earth and Planetary Sciences, 36, 389-420.

González, F. J., Somoza, L., Lunar, R., Martínez-Frías, J., Rubí, J. A. M., Torres, T., Ortiz, J. E., and Díaz-del-Río (2010). Internal features, mineralogy and geochemistry of ferromanganese nodules from the Gulf of Cadiz: The role of the Mediterranean Outflow Water undercurrent. Journal of Marine Systems, 80, 203-218.

Hein, J. R., Koschinsky, A., and Halliday, A. N. (2003). Global occurrence of tellurium-rich ferromanganese crusts and a model for the enrichment of tellurium. Geochimica et Cosmochimica Acta, 67, 1117-1127.

Huebner, S., and Flohr, M.J.K. (1990). Microbanded Manganese Formations: Protoliths in the Franciscan Complex, California. U.S. Geological Survey Professional Paper 1502, United States Government Printing Office, Washington, 72p.

Kawachi, Y., Grapes, R. H., Coombs, D. S., and Dowse, M. (1983). Mineralogy and petrology of a piemontite-bearing schist, western Otago, New Zealand. Journal of Metamorphic Geology, 1, 353-372.

Kelley, K.A., and Cottrell, E. (2009). Water and the Oxidation State of Subduction Zone Magmas. Science, 325, 605-607.

Lee, C.-T.A., Luffi, P., Le Roux, Dasgupta, R., Albarede, F., and Leeman, W.P., 2010. The redox state of arc mantle using Zn/Fe systematics. Nature, 468, 681-685.

Li, J.-L., Schwarzenbach, E. M., John, T., Ague, J. J., Huang, F., Gao, J., Klemd, R., Whitehouse, M. J., and Wang, X.-S. (2020). Uncovering and quantifying the subduction zone sulfur cycle from the slab perspective. Nature Communications, 11, 514.

Malaspina, N., Langenhorst, F., Tumiati, S., Campione, M., Frezzotti, M. L., and Poli, S. (2017). The redox budget of crust-derived fluid phases at the slab-mantle interface. Geochimica Et Cosmochimica Acta, 209, 70-84.

März, C., Stratmann, A., Matthiessen, J., Meinhardt, A. K., Eckert, S., Schnetger, B., Vogt, C., Stein, R., and Brumsack, H. J. (2011). Manganese-rich brown layers in Arctic Ocean sediments. Composition, formation mechanisms, and diagenetic overprint. Geochimica et Cosmochimica Acta, 75, 7668-7687.

McCammon, C.A., Frost, D.J., Smyth, J.R., Laustsen, H.M.S., Kawamoto, T., Ross, N.L., and van Aken, P.A. (2004). Oxidation state of iron in hydrous mantle phases: implications for subduction and mantle oxygen fugacity. Physics of the Earth and Planetary Interiors 143–144, 157-169.

Mero, J. L. (1965). The mineral resources of the sea. Elsevier Oceanography Series, 312p.

Narejo, A. A., Shar, A. M., Fatima, N., and Sohail, K. (2019). Geochemistry and origin of Mn deposits in the Bela ophiolite complex, Balochistan, Pakistan. Journal of Petroleum Exploration and Production Technology, 9, 2543-2554

Ni, H., Zhang, L., Xiong, X., Mao, Z., and Wang, J. (2017). Supercritical fluids at subduction zones: Evidence, formation condition, and physicochemical properties. Earth-Science Reviews, 167, 62-71.

Parkinson, I.J., and Arculus, R.J. (1999). The redox state of subduction zones: insights from arc-peridotites. Chemical Geology, 160, 409-423.

Poli, S., and Schmidt, M. W. (2002). Petrology of subducted slabs. Annual Review of Earth and Planetary Sciences, 30, 207-235.

Post, J.E. (1999). Manganese oxide minerals. Crystal structures and economic and environmental significance. Proceedings of the National Academy of Sciences, 96, 3447-3454.

Rajabzadeh, M. A., Haddad, F., Polgári, M., Fintor, K., Walter, H., Molnár, Z., and Gyollai, I. (2017). Investigation on the role of microorganisms in manganese mineralization from Abadeh-Tashk area, Fars Province, southwestern Iran by using petrographic and geochemical data. Ore Geology Reviews, 80, 229-249.

Richards, J. P. (2015). The oxidation state, and sulfur and Cu contents of arc magmas: implications for metallogeny. Lithos, 233, 27-45.

Rona, A. (2008). The changing vision of marine minerals. Ore Geology Reviews, 33, 618-666.

Song, S.G., Niu, Y.L., Su, L., and Xia, X.H. (2013). Tectonics of the North Qilian orogen, NW China. Gondwana Research, 23, 1378-1401.Song, S.G., Zhang, L.F., Niu, Y.L., Wie, C.J., Liou, J.G., and Shu, G.M. (2007). Eclogite and carpholite-bearing metasedimentary rocks in the North Qilian suture zone, NW China: implications for early palaeozoic cold oceanic subduction and water transport into mantle. Journal of Metamorphic Geology, 25, 547-563.

Song, S. G., Niu, Y. L., Su, L., Zhang, C., and Zhang, L. F. (2014). Continental orogenesis from ocean subduction, continent collision/subduction, to orogen collapse, and orogen recycling: The example of the North Qaidam UHPM belt, NW China. Earth-Science Reviews, 129, 59-84.

Song, S. G., Yang, L. M., Zhang, Y. Q., Niu, Y. L., Wang, C., Su, L. and Gao, Y. L. (2017). Qi-Qin Accretionary Belt in Central China Orogen: accretion by trench jam of oceanic plateau and formation of intra-oceanic arc in the Early Paleozoic Qin-Qi-Kun Ocean. Science Bulletin, 62, 1035-1038.

Vrána, S. (2011). Manganese-rich garnet-quartz rocks and gneisses in the Bohemian part of the Moldanubian Zone: Lithostratigraphic markers. Journal of Geosciences, 56, 359–374.

Whitney, D. L. and Evans, B. W. (2010). Abbreviations for names of rock-forming minerals. American Mineralogist 95, 185-187.

Willner, A.P., Pawlig, S., Massonne, H.J., and Hervé, F. (2001). Metamorphic evolution of spessartine quartzites (coticules) in the high-pressure, low-temperature complex at Bahia Mansa, Coastal Cordillera of south-central Chile. Canadian Mineralogist, 39, 1547–1569.

Tahir Shah, M. Khan, A. (1999). Geochemistry and origin of Mn-deposits in the Waziristan ophiolite complex, north Waziristan, Pakistan. Mineralium Deposita, 34, 697-704.

Tahir Shah, M., and Moon, C. J. (2007). Manganese and ferromanganese ores from different tectonic settings in the NW Himalayas, Pakistan. Journal of Asian Earth Sciences, 29, 455-465.

Tumiati, S., Martin, S., Godard, G. (2010). Hydrothermal origin of manganese in the highpressure ophiolite metasediments of Praborna ore deposit (Aosta Valley, Western Alps). European Journal of Mineralogy, 11, 577–594.

Tumiati, S., Godard, G., Martin, S., Malaspina, N., and Poli, S. (2015). Ultra-oxidized rocks in subduction mélanges? Decoupling between oxygen fugacity and oxygen availability in a Mn-rich metasomatic environment. Lithos, 226, 116-130.

Wei, C. J., and Song, S. G. (2008). Chloritoid-glaucophane schist in the north Qilian orogen, NW China: phase equilibria and P-T path from garnet zonation. Journal of Metamorphic Geology, 26, 301-316.

Wood, B.J., Bryndzia, L.T., and Johnson, K.E. (1990). Mantle Oxidation State and Its Relationship to Tectonic Environment and Fluid Speciation. Science, 248, 337-345.

Xia, X. H., Song, S. G., and Niu, Y. L. (2012). Tholeiite-Boninite terrane in the North Qilian suture zone: Implications for subduction initiation and back-arc basin development. Chemical Geology, 328, 259-277.

Ye, S.T., Song S.G., and Chen, J. (2019). Mineralogy of ardennite-(As) from HP metamorphic Mn-rich silica rocks in North Qilian Mountain. Acta Petrologica et Mineralogica, 38, 90-96 (in Chinese with English abstract).

Zhang, J.X., Meng, F.C., and Wan, Y.S., (2007). A cold Early Palaeozoic subduction zone in the North Qilian Mountains, NW China: petrological and U-Pb geochronological constraints. Journal of Metamorphic Geology, 25, 285-304.

## Figure Captions

**Fig. 1. (a)** Geological maps of the North Qilian suture zone (modified after Song et al., 2007). (b) Qingshuigou section of the HP subduction complex with locations of Mn-rich cherts. (c) Deformed Mn-rich chert (Mn-rich quartzite schist). (d) Fe-Mn nodule (black) surrounded by pyroxmangite (Pxm) (pink). (e) Pxm+Grt (pink) with hematite (Hem) band. (f) Banded hematite -aegirine quartzite. Mineral Abbreviations are after Whitney and Evans (2010).

**Fig. 2.** Photomicrographs of Mn-Fe high-pressure cherts in the North Qilian orogeny. (a) BSE image of syn-kinetic garnet with hematite in the Mn-rich quartz schist. Note that this rock was strongly

deformed, suggesting a syn-tectonic high-pressure metamorphism. (b) Jadeite (Jd) in the Mn-rich quartz schist. (c) Grt + Pxm + Hem in the nodule-bearing quartzite. All minerals are euhedral without deformation. (d) Aegirine (Aeg) in the banded Fe-Mn-rich quartzite. (e) BSE image of euhadral hematites with minor sussexite in the banded Fe-Mn-rich quartzite. Note that the rock did not experience deformation during HP metamorphism. (f) Ardennite-(As) (Ard) with sursassite (Srs) and piedmontite in the Mn-rich quartz schist.

**Fig. 3.** Composition diagrams for garnets (a) and sodic clinopyroxenes (b). Note that all garnet and sodic clinopyroxene have calculated $Fe^{3+}/\Sigma Fe$ ratios of 1.

**Fig. 4.** Raman spectra for ferromanganese-rich minerals in the HP cherts (see description in the text for details).

**Fig. 5.** A schematic diagram showing circulation of oxygen and water with redox reactions of manganese and iron in the ocean floor and the subduction zone. Oxygen would further react with organic carbon and sulfite, or as the supercritical fluids transporting to the mantle wedge.

**Table 1**. Representative metamorphic Mn-rich cherts within global ophiolite and subducted mélange belts

**Table 1**. Representative metamorphic Mn-rich cherts within global ophiolite and subducted mélange belts*

| Location | Rock assemblage | Mineral assemblages | P-T conditions | References |
|---|---|---|---|---|
| Qilian Orogen | Fe-Mn Chert in ophiolitic mélange, eclogite, blueschist | Garnet, omphacite-jadeite-aegirine, pyroxmangite, piedmontite, phengite, glaucophene, hematite, ardennite | P=2.0-2.6 GPa T=450-550 °C | This study |
| Praborna Mn-ore Deposit, Zermatt-Saas, Western Alps | Fe-Mn Chert in meta-ophiolites, eclogite, blueschist, | Garnet, omphacite-jadeite-aegirine, pyroxmangite, braunite, piedmontite, phengite, glaucophene, hematite, ardennite | P = 2.1±0.3 GPa T = 550± 60°C | Tumiati et al., 2010, 2015 |
| St. Marcel, Piedmont, Italy | Meta-chert in blueschists | Diopside-omphacite-albite-quartz, braunite, microcline, hollandite, piedmontite, phengite, quartz | P = 0.8 ± 0.1 GPa T = 300 ± 50 °C | Brown et al., 1978 |
| Sanbagawa Metamorphic Belt, central Shikoku, Japan | Piemontite quartz schist with blueschist and eclogite | Grt, aegirine-augite, sodic-amphibole, piemontite, phengite, braunite, albite, hematite, talc, crossite | P = 1.0–1.2 GPa T = 300-600 °C | Izadyar et al., 2000 |
| Eastern Hokkaido, Japan | The piemontite-bearing chert | Piemontite, pumpellyite, hematite, quartz | P > 0.8 GPa T< 400~450 °C | Akasaka et al., 1988 |
| Otago, New Zealand | Fe-Mn quartzose schist in ophiolitic mélange complex | Garnet, phengite, albite, coombsite, zussmanite, parsettensite, caryopilite, hematite, rutile, quartz | P = 0.64 GPa T = 400 °C | Kawachi et al., 1983 |
| Buckeye, Franciscan Complex, USA | Mn-deposit in bedded chert. | Rhodochrosite, gageite, hausmannite, braunite, caryopilite, taneyamalite, chlorite, hematite, aegirine-augite, quartz | Blueschist/Greenschist facies | Huebner and Flohr, 1990, 1992 |
| Paleo-Tethyan, Karakaya and Neo-Tethyan suture belts, Turkey | Mn-deposits in cherts in ophiolitic mélange zones | braunite, bixbyite, psilomelane, Mn-calcite, hematite, quartz, chlorite, zeolite | Greenschist to sub-greenschist facies | Öztürk, 1997 |
| Waziristan and Bela, Pakistan | Mn-Fe rich chert and Mn-deposits in ophiolites | Braunite, psilomelane, hematite, quartz | Sub-greenschist facies | Tahir Shah and Khan, 1999 Tahir Shah and Moon, 2007 Narejo et al., 2019 |
| Abadeh-Tashk area, Fars Province, Iran | Mn-deposits in Neyriz ophiolite mélange, | Psilomelane, braunite, hollandite, birnessite, todorokite, pyrolusite, rancieite, pyrochroite, hematite, quartz, aurorite, rancieite | Sub-greenschist facies | Rajabzadeh et al., 2017 |

*Note: The low-grade metamorphosed Mn-deposits from ophiolites are dominated by $Mg^{4+}$ and $Mg^{3+}$ minerals, and change systematically from Mn4+ to Mn2+ with the progression of metamorphic grades.

# Fig. 1

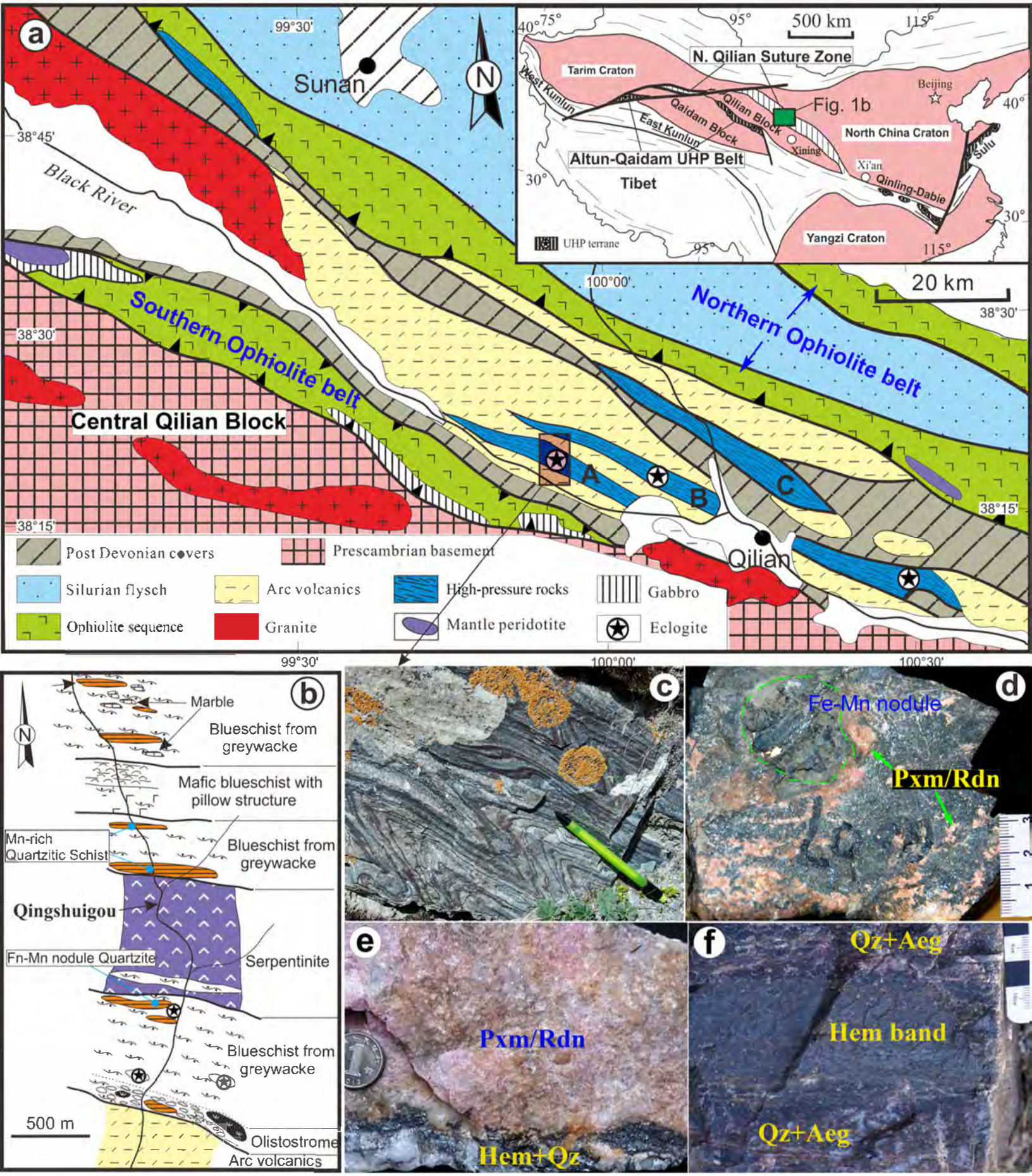
a
99°30'
Sunan
N
38°45'
Black River
Southern Ophiolite belt
38°30'
Central Qilian Block
38°15'
100°00'
Northern Ophiolite belt
38°30'
A
B
C
38°15'
Qilian
99°30'
100°00'
100°30'
Post Devonian covers
Prescambrian basement
Silurian flysch
Arc volcanics
High-pressure rocks
Gabbro
Ophiolite sequence
Granite
Mantle peridotite
Eclogite
500 km
N. Qilian Suture Zone
Tarim Craton
West Kunlun
East Kunlun
Qaidam Block
Qilian Block
Fig. 1b
Beijing
North China Craton
Xining
Xi'an
Qinling-Dabie
Sulu
Altun-Qaidam UHP Belt
Tibet
Yangzi Craton
UHP terrane
20 km
b
Marble
Blueschist from greywacke
Mafic blueschist with pillow structure
Mn-rich Quartzitic Schist
Blueschist from greywacke
Qingshuigou
Fn-Mn nodule Quartzite
Serpentinite
Blueschist from greywacke
500 m
Olistostrome
Arc volcanics
c
d
Fe-Mn nodule
Pxm/Rdn
e
Pxm/Rdn
Hem+Qz
f
Qz+Aeg
Hem band
Qz+Aeg

**Fig 2**

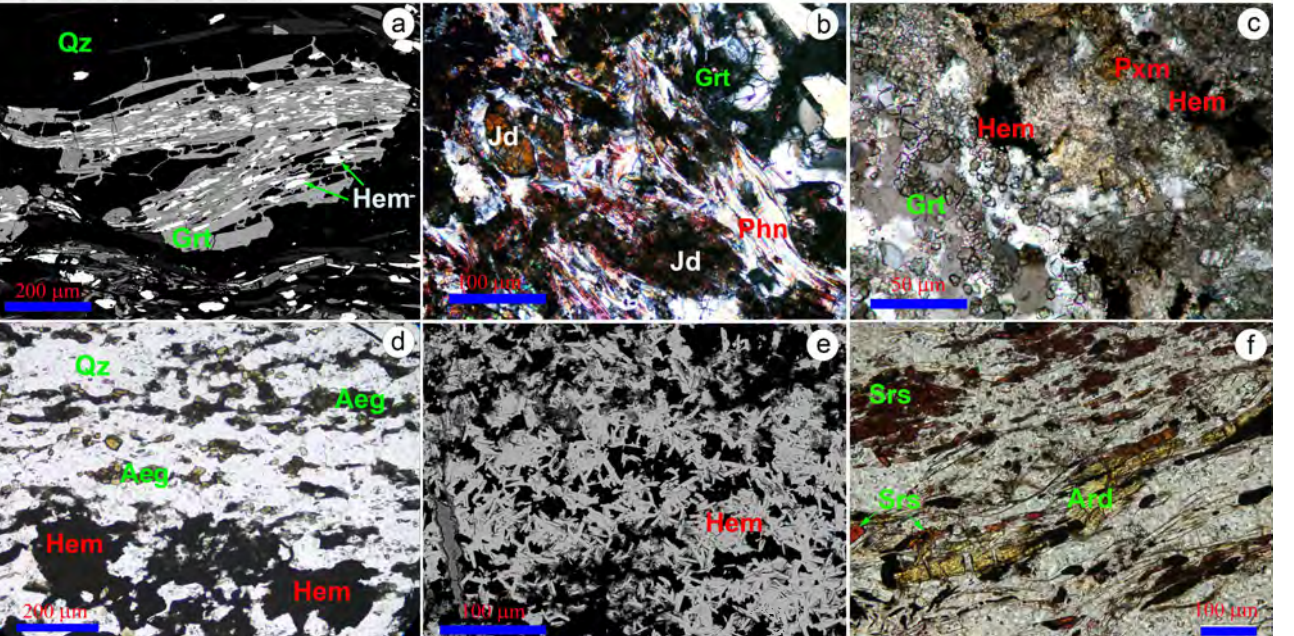
a
Qz
Hem
Grt
200 µm
b
Grt
Jd
Phn
Jd
100 µm
c
Pxm
Hem
Hem
Grt
50 µm
d
Qz
Aeg
Aeg
Hem
Hem
200 µm
e
Hem
100 µm
f
Srs
Srs
Ard
100 µm

**Fig 3**

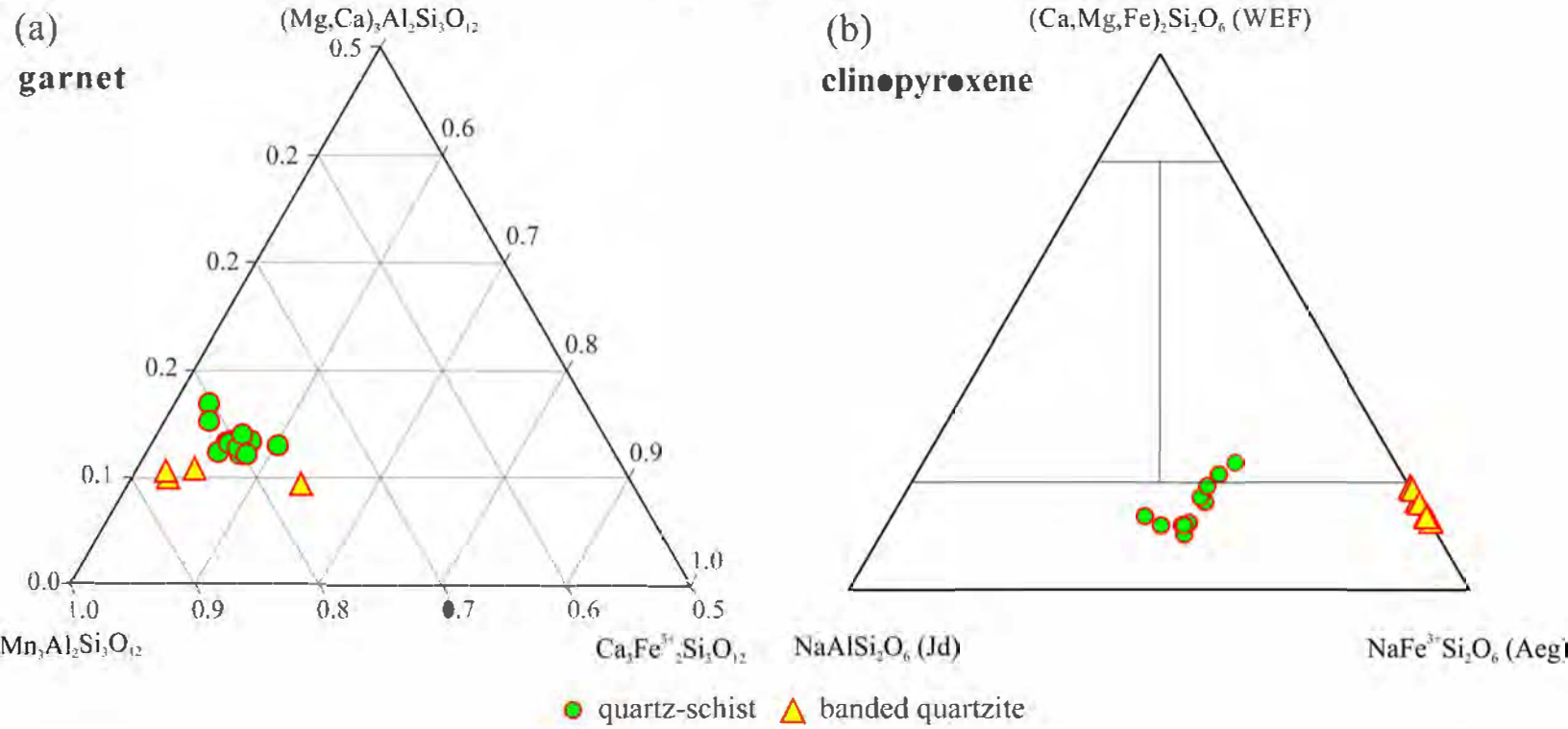
(a)
garnet
(Mg,Ca)3Al2Si3O12
0.5
0.6
0.7
0.8
0.9
1.0
0.2
0.2
0.2
0.1
0.0
1.0
0.9
0.8
0.7
0.6
0.5
Mn3Al2Si3O12
Ca3Fe3+2Si3O12
(b)
clinopyroxene
(Ca,Mg,Fe)2Si2O6 (WEF)
NaAlSi2O6 (Jd)
NaFe3+Si2O6 (Aegi
quartz-schist
banded quartzite

# Fig 4

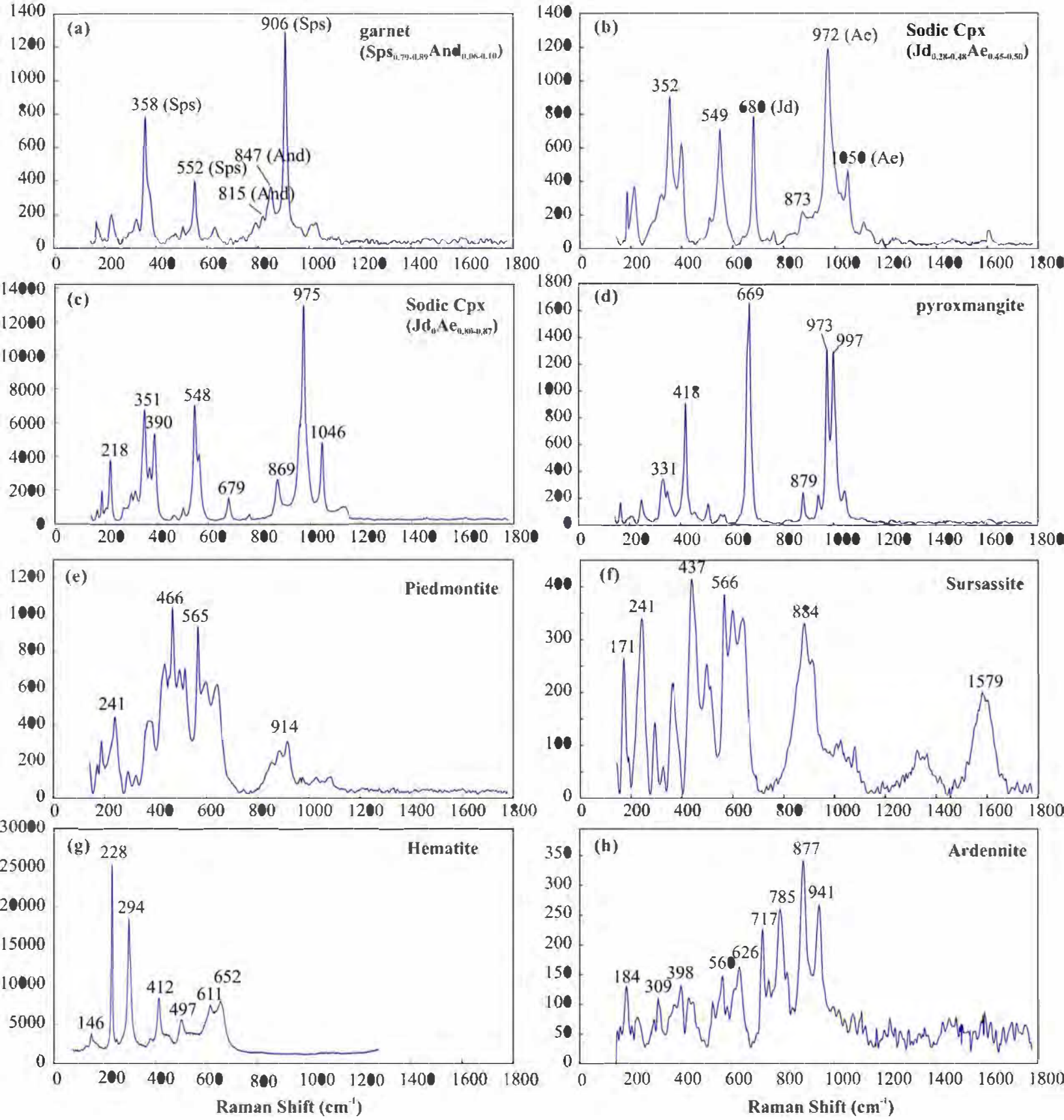
(a)
garnet
(Sps0.79-0.89And0.08-0.10)
906 (Sps)
358 (Sps)
552 (Sps)
847 (And)
815 (And)
(b)
Sodic Cpx
(Jd0.28-0.48Ae0.45-0.50)
972 (Ae)
352
549
680 (Jd)
1050 (Ae)
873
(c)
Sodic Cpx
(Jd0Ae0.93-0.87)
975
351
390
548
218
679
869
1046
(d)
pyroxmangite
669
973
997
418
331
879
(e)
Piedmontite
466
565
241
914
(f)
Sursassite
437
566
241
884
171
1579
(g)
Hematite
228
294
412
652
611
497
146
(h)
Ardennite
877
785
941
717
626
560
398
184
309
Raman Shift (cm-1)
Raman Shift (cm-1)

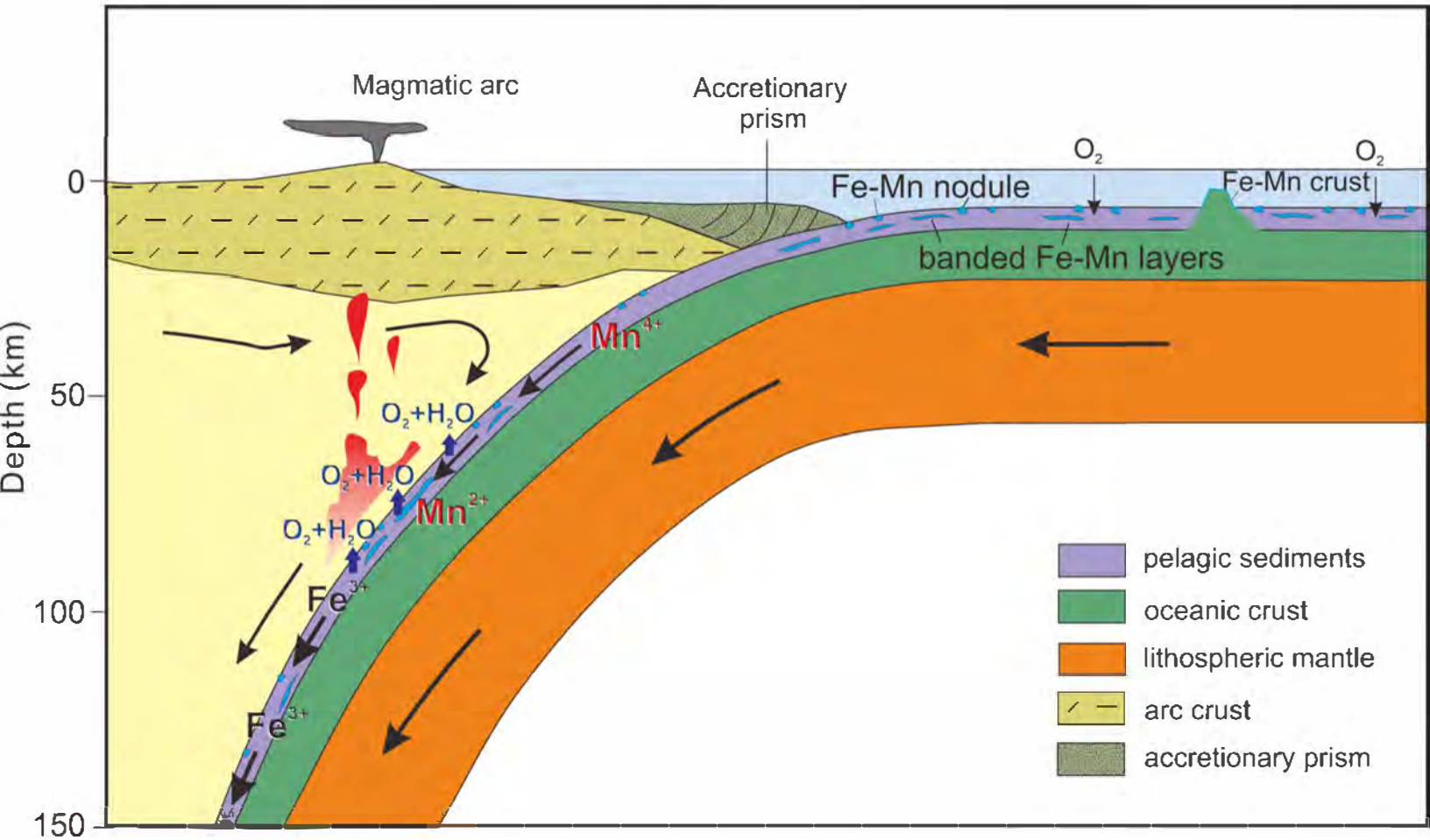
Magmatic arc
Accretionary prism
$O_2$
$O_2$
Fe-Mn nodule
Fe-Mn crust
banded Fe-Mn layers
$Mn^{4+}$
$O_2+H_2O$
$O_2+H_2O$
$O_2+H_2O$
$Mn^{2+}$
$Fe^{3+}$
$Fe^{3+}$
Depth (km)
0
50
100
150
pelagic sediments
oceanic crust
lithospheric mantle
arc crust
accretionary prism